Supplementary material: Topological Wannier cycles for the bulk and edges

Ze-Lin Kong(孔泽霖) [1] , Zhi-Kang Lin(林志康) [1*] , and Jian-Hua Jiang(蒋建华) [1,2*]

[1]School of Physical Science and Technology, and Collaborative Innovation Center of Suzhou Nano Science and Technology, Soochow University, Suzhou 215006, China

[2]Key Lab of Advanced Optical Manufacturing Technologies of Jiangsu Province, and Key Lab of Modern Optical Technologies of Ministry of Education, Soochow University, Suzhou 215006, China

* Email : linzhikangfeynman@163.com; jianhuajiang@suda.edu.cn

Text A: Illustration of creating the single-plaquette artificial gauge flux

We insert the single-plaquette artificial gauge flux from three consecutive procedures. These procedures are illustrated in Fig. S1. The first procedure is dimension extension. For instance, the two-dimensional (2D) breathing kagome model is stacked along the z-direction periodically to extend the system from a 2D model to a three-dimensional (3D) model. Note that here the coupling in the z-direction is not essential. We, in fact, consider the limit that the coupling along the z-direction vanishes. We then create a step screw dislocation (SSD) at the center of these dimension-extended systems. We specifically consider systems that are finite in the original dimensions but periodic in the z-direction. Here, the step screw dislocation consists of three flat sectors ("steps"). But the couplings between the adjacent sectors are tilted in such a way that these flat steps form a screw dislocation with a clear chirality and an emergent screw symmetry $S_{3z} = C_3 * \mathcal{L}_z(\frac{1}{3})$ with $\mathcal{L}_z(\frac{1}{3}) := z \to z + \frac{1}{3}$. The third procedure is dimension reduction by the Fourier transformation along the z-direction, which splits the system into several 2D systems labeled by k_z.
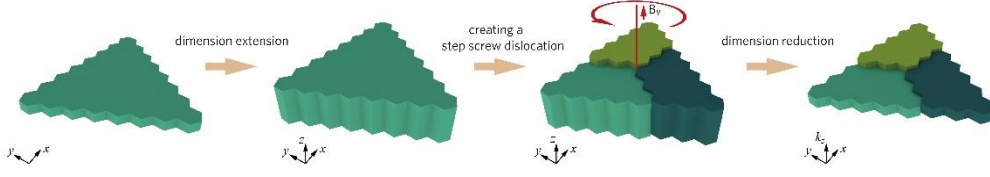
Figure S1 : (Color online) Schematic illustration of the three consecutive procedures that are used to create the artificial gauge flux: dimension extension, creating a step screw dislocation and dimensional reduction.

Text B: Topological indexes, elementary band representations and charge distributions

Following Ref. [1], as the breathing kagome and SSH models separately respect C_3 and C_2 point group symmetries, the topology of their bulk band gaps can be detected, respectively, by the following topological indexes

$$\chi^{(3)} = \left(\left[K_1^{(3)}\right], \left[K_2^{(3)}\right]\right); \ \chi^{(2)} = \left(\left[X_1^{(2)}\right], \left[Y_1^{(2)}\right], \left[M_1^{(2)}\right]\right), \qquad (1)$$

where $\left[\Pi_p^{(n)}\right] = \#\Pi_p^{(n)} - \#\Gamma_p^{(n)}$, $\#\Pi_p^{(n)}$ denotes the number of bulk bands below the band gap with C_n symmetry eigenvalue $e^{ip(2\pi/n)}$ at Π point, $p = 0, 1, \dots, n-1$ and Π stands for K in the breathing kagome lattice and X, Y and M for the SSH lattice.

Based on the little group representations labeled in Fig. 1 in the main text and the character tables of C_3 and C_2 groups (see Table. S1), we can directly acquire the rotation eigenvalues of these representations. Then, the topological indexes of bulk band gaps can be calculated. For the topological phase, the topological indexes are $\chi^{(3)} = (1,0)$ and $\chi^{(2)} = (-1, 0, -1)$, respectively, for the breathing kagome and SSH lattices, while $\chi^{(3)} = (0,0)$ and $\chi^{(2)} = (0, 0, 0)$, for the trivial phase.

The Wannier orbitals located at the Wyckoff positions in real space and the little group representations (or symmetry eigenvalues) of eigenstates at high-symmetry points in the Brillouin zone are related by the theory of elementary band representations (EBRs). The EBRs of P_3 and P_2 space groups are given in Table. S1, where g_n

denotes the rotation eigenvalues of Wannier orbitals, and the subscripts a, b, and c represent the Wyckoff positions. The EBRs support the analysis of Wannier orbitals and centers in the main text.

The distributions of electron charges of the finite systems, as given in Figs. 4(c) and 4(d) of the main text, are obtained in a simple way by evaluating the proportion of bulk Wannier centers falling in each unit-cell. One can also use the first principle method to calculate the electron charges in each unit-cell,

$$Q = \int_0^{\epsilon_{gap}} d\epsilon \int_{u.c.} dr \rho(\epsilon, r), \qquad (2)$$

where ϵ_{gap} is the upper limit of the energy integration, which should be placed above the lower-energy bulk states. The integration over the site coordinates r is performed over one unit-cell as denoted by $u.c.$. $\rho(\epsilon, r)$ is the local density of states (LDOS) of electrons depending on the energy ϵ and the coordinate r, which can be written as

$$\rho(\epsilon, r) = \sum_i \frac{\Gamma}{\pi |\Gamma^2 + (\epsilon - \epsilon_i)^2|} |w_i(r)|^2, \qquad (3)$$

where $w_i(r)$ is the wave function of the i-th eigenstate with the normalization $\int_{u.c.} dr |w_i(r)|^2 = 1$. Γ is a sufficiently small parameter to model the Lorentz broadening. We remark that the corner and edge states calculated from the first-principle method deviate from the values labeled in Figs. 4(c) and 4(d) of the main text. The latter depicts the charge distributions in the limit with extremely localized Wannier orbitals.

(a)

irreps	E	C_3^+	C_3^-
A	1	1	1
^1E	1	$e^{-i2\pi/3}$	$e^{i2\pi/3}$
^2E	1	$e^{i2\pi/3}$	$e^{-i2\pi/3}$

(b)

irreps	E	C_2
A	1	1
B	1	-1

(c)

EBRs	Γ	K
$(g_0)_a$	A	A
$(g_0)_b$	A	^1E
$(g_0)_c$	A	^2E
$(g_1 \oplus g_2)_a$	E	$^1E\,^2E$
$(g_1 \oplus g_2)_b$	E	$A \oplus {}^1E$
$(g_1 \oplus g_2)_c$	E	$A \oplus {}^2E$

(d)

EBRs	Γ	X	M	Y
$(g_0)_a$	A	A	A	A
$(g_0)_b$	A	B	B	A
$(g_1)_a$	B	B	B	B
$(g_1)_b$	B	A	A	B

Table S1: (a) and (b). Character tables of C_3 and C_2 point group symmetries, respectively. (c) and

(d) Elementary band representations of the P_3 and P_2 space group symmetries. g_n denotes the rotation eigenvalues of Wannier orbitals, the subscripts a, b, and c label the Wyckoff positions.

Text C: Realization of Wannier cycles in phononic systems via sonic crystals

We simulate the phononic realization of the studied breathing kagome and SSH lattices in the main text. by using the commercial software COMSOL Multiphysics. In terms of the tight-binding (TB) models, the phononic models are realized by connected acoustic resonators which are cylindrical cavities with the height $h = 0.5a$ and the diameter $D = 0.3a$, where a is the lattice constant. The transmission of sound along each tube connecting them denotes the nearest-neighbor hoppings, whose strength is controlled by the diameter of the tube. Specifically, to obtain the nontrivial band topology, we use tubes of the diameter $d_1 = 0.1a$ ($d_2 = 0.2a$) to realize the intra-unit-cell (inter-unit-cell) hoppings. The unit-cells of the phononic models are illustrated in Figs. S2(a) and S2(b). Here, for simplicity, we set $t_3 = 0$ in the SSH lattice. The phononic topological bulk bands are shown in Figs. S2(c) and S2(d), in units of the frequency v/a (v is the sound velocity in air). The little group representations at high-symmetry points are also exhibited, which are deduced from their corresponding phase distribution of wavefunctions, as given in the insets. All these representations are the same as those of TB models shown in Fig. 1 in the main text.

We then calculate the spectra as functions of the inserted single-plaquette artificial gauge flux for the breathing kagome and SSH models with a step screw dislocation, as presented in Fig. S3. The results confirm the emergence of the topological Wannier cycles in realistic materials which are also confirmed in a recent experimental study (see Ref. [2]). In fact, these numerical results are even more encouraging: Due to the absence of the chiral symmetry in these phononic systems, the edge and corner states disappear in the phononic realization. However, even in this situation, the topological Wannier cycle still emerges and can thus serve as a reliable experimental signature of higher-order band topology and the filling anomaly. In fact, the breaking of the chiral symmetry is common in higher-order topological materials. Such an effect imposes

challenges for experimental detection of the higher-order band topology. The topological Wannier cycle then serves as an unprecedented way to solve such a problem.
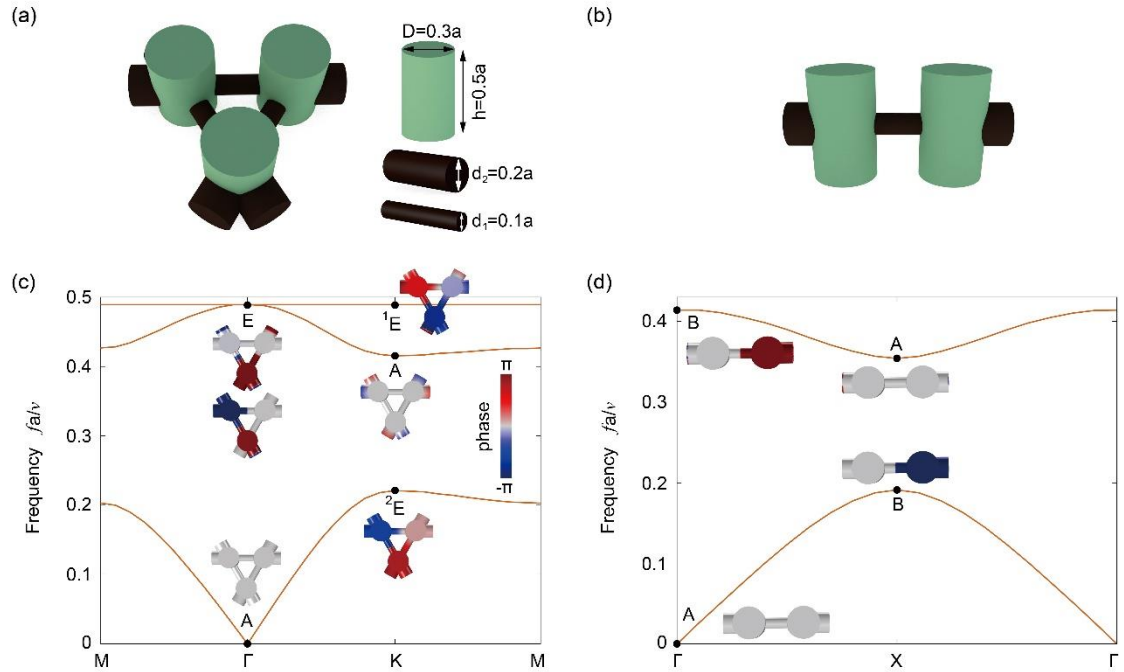

Figure S2: (Color online) Phononic realization of the breathing kagome and SSH lattices. (a) Unit-cell of the phononic breathing kagome model in topological phase. The right panel shows that a site is realized by a cylindrical acoustic resonator with the diameter $D = 0.3a$ and the height $h = 0.5a$, while the intra- and inter-unit-cell couplings are realized by the tubes of diameters $d_1 = 0.1a$ and $d_2 = 0.2a$, respectively. (b) Unit-cell of the phononic SSH model in topological phase. (c) and (d) Corresponding phononic bulk band structures for (a) and (b). Inset shows the little group representations at high-symmetry points associated with phase patterns of their wavefunctions.
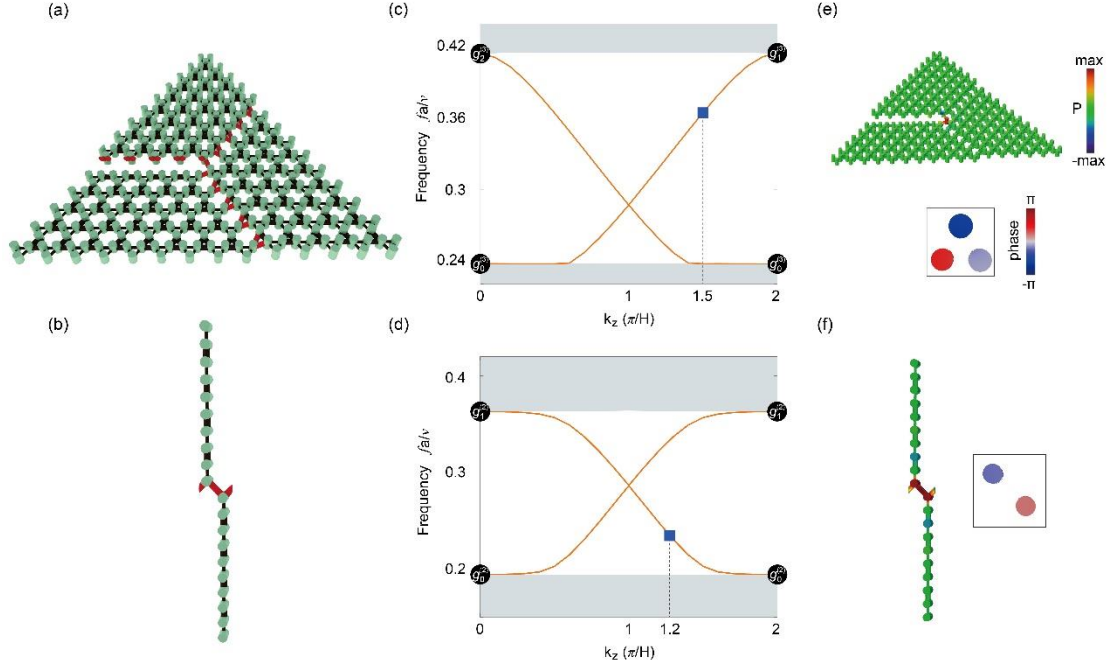
Figure S3: (Color online) Phononic realization of the artificial gauge flux insertion in a single plaquette and topological Wannier cycles. (a) and (b): The designed sonic crystal structures for (a) the breathing kagome model and (b) the SSH model when the procedures in Fig. S1 are applied. The red tubes denote the slanted couplings between the adjacent sectors. (c) and (d) The corresponding phononic spectra as functions of $\Phi = k_z H$ for the structures in (a) and (b). The grey region denotes the bulk states. The orange curves represent the spectral flows across the band gaps. (e) and (f) The phononic wavefunctions of in-gap states, marked by blue squares in (c) and (d), are localized around the local gauge flux at the central plaquette. The phase patterns around central acoustic resonators validate the Wannier cycles.

Text D: Topological Wannier cycles of edge states in the quadrupole model

We in the main text extend the topological bulk Wannier cycles to the edge Wannier cycles by creating a step glide dislocation in the 2D SSH model. Nevertheless, there are always accompanied spectral flows of bulk states in the band gap. Here, we achieve the topological Wannier cycles of only edge states, by replacing the 2D SSH model with the 2D quadrupole model. As illustrated in Fig. S4(a), the difference compared to the 2D SSH model is that the quadrupole model has negative couplings $-t_1$ and $-t_2$, as denoted by the cyan lines. The negative couplings leave all the energy bands twofold-

degenerate in the Brillouin zone and make the corner states observable in the spectra at the zero energy. Here, the key to getting rid of the topological Wannier cycles of bulk states is that, due to the twofold degeneracy, the bulk continua always have an even number of states. Under the gauge flux, the cyclic transformation between bulk eigenstates with rotation eigenvalues $g_0^{(2)}$ and $g_1^{(2)}$ can be fulfilled within each bulk continuum. Hence, only the topological Wannier cycles of edge states persist, as denoted by the red curves in the spectra in Fig. S4(b).
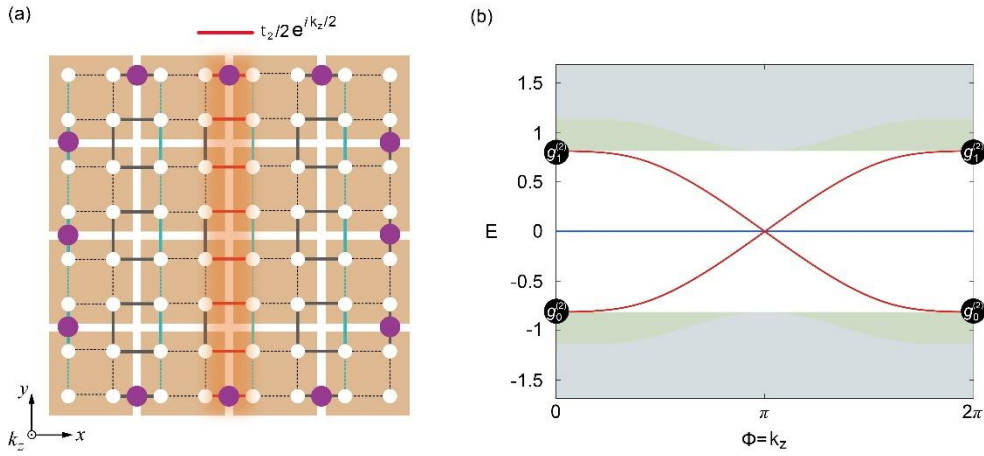

Figure S4: (Color online) Topological Wannier cycles of edge states. (a) The effective TB 2D quadrupole model with a step glide dislocation. The dashed and solid lines denote the intra- and inter-unit-cell couplings t_1 and t_2, respectively. The cyan lines denote the negative couplings. The purple dots denote the Wannier centers in the edge regions. The orange zone represents the gauge flux. (b) The corresponding energy spectra in (a) as functions of the gauge flux k_z. The grey and cyan zones denote the bulk and edge states, respectively. The spectral flows of edge states are marked with red color. The blue line denotes the corner states. The TB parameters are the same as those in Fig. 5(b) in the main text.

Text E: Robustness of Wannier cycles

In this section, we study the robustness of the Wannier cycles against various disorders in TB models. As shown in Fig. S5, we introduce disorders by means of

double enhancing or half weakening some hopping strength located away from the center (blue region), near the center (green region), and at the very center (red region) of the two-dimensional kagome and SSH lattices with artificial gauge fields. Particularly, all these disorders preserve the rotation symmetry, C_3 or C_2, to protect the gapless feature of spectral flows. As shown in Figs. S5(b) and S5(f), the disorders away from the center, despite the stronger or weaker hopping strength, have almost no effects on the dispersion of spectral flows, which makes sense because these disorders barely overlap with the center-localized states manifested by spectral flows. The disorders near the center with weak hopping strength [left panel in Figs. S5(c)] introduce other localized states in the breathing kagome model, which mix with the spectral flows but do not alter the gapless feature. The disorders at the very center with weaker hoppings [left panel in Figs. S5(d)] shift the spectral flow with higher energy and make them away from the lower bulk states. For the SSH model, The disorders near and at the center both "compress" the dispersion which makes the spectral flows isolated in energy. The disorders at the very center with stronger hoppings only slightly alter the dispersion and do not affect their energy range and gapless feature.
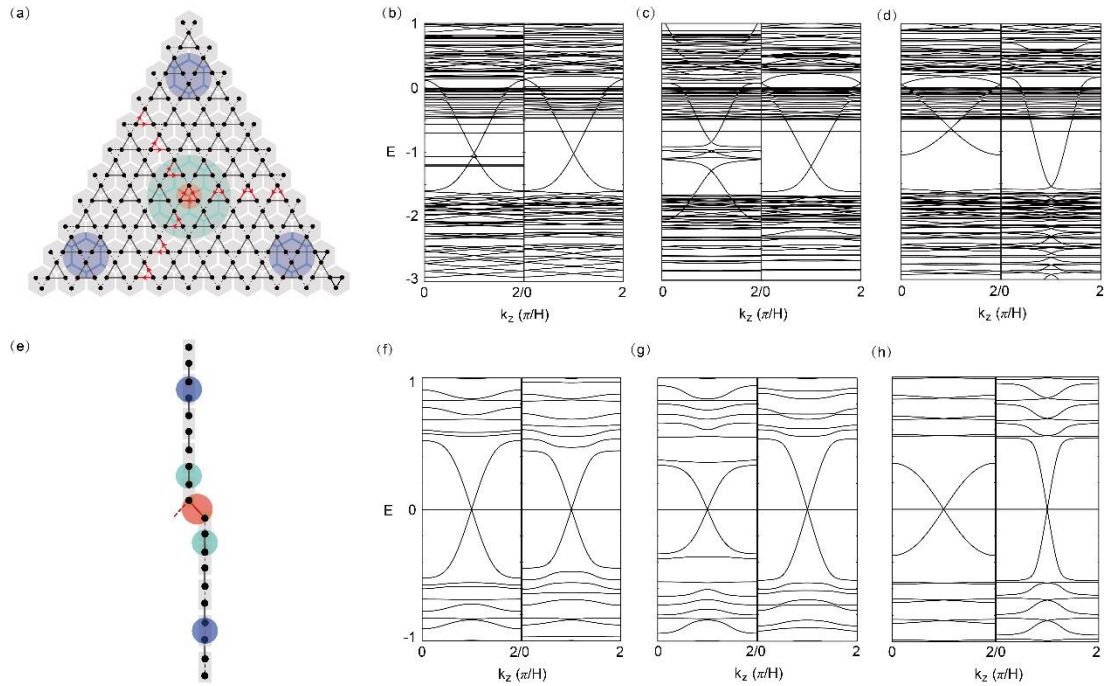

Figure S5: (Color online) Robustness of the Wannier cycles. (a) The effective breathing kagome TB model with disorders located away from the center (blue region), near the center (green

region), and at the very center (red region). (b)-(d) Spectra as functions of $\Phi = k_z H$ for the structures in (a) with disorders located away from the center, near the center and at the very center. The Left and right panels correspond to weaker and stronger hoppings in disorders, respectively. (e)-(h) Similar to (a)-(d) but for the SSH lattice.

References

[1] Benalcazar W A, Li T and Hughes T L 2019 *Phys. Rev. B* **99** 245151

[2] Lin Z K, Wu Y, Jiang B, Liu Y, Wu S, Li F and Jiang J H 2022 *Nat. Mater.* **21**. 430-437